Variational Mode Decomposition-based Synchronous Multi-Frequency Electrical Impedance Tomography

Qing-Xin Pan, Yang Li, Nan Wang, Peng-Fei Zhao

College of Information and Electrical Engineering, China Agricultural University, Beijing 100083, China;
e-mail: hlan@cau.edu.cn

Lan Huang, Zhong-Yi Wang

College of Information and Electrical Engineering, China Agricultural University, Beijing 100083, China;
e-mail: hlan@cau.edu.cn.

Key Laboratory of Modern Precision Agriculture System Integration Research, Ministry of Education,
Beijing 100083, China

Key Laboratory of Agricultural Information Acquisition Technology, Ministry of Agriculture,
Beijing 100083, China

Corresponding author: hlan@cau.edu.cn

Electrical impedance tomography (EIT) can provide the system structure and functional imaging ability needed to map the distribution of and changes in plant root zones in a non-invasive, low-cost, safe, fast, and simple manner. Multi-frequency EIT solves the problem that single-frequency EIT can only carry impedance infor-

mation corresponding to a single given excitation frequency. However, performing EIT at multiple frequencies simultaneously remains challenging. To address this problem, a mixed signal in which multiple frequencies are superimposed is injected into the object to be measured. Essentially, the aim of this approach is to separate the measured mixed voltage signals and thus acquire electrical impedance information simultaneously and quickly at various frequencies. Because the measured signal is a multi-frequency signal, decomposing this signal affects the imaging accuracy directly. To acquire more accurate data, the variational mode decomposition (VMD) method is used to decompose the measured multi-frequency signal. Accurate amplitude and phase information can be obtained simultaneously via multi-frequency excitation, and these data are then used to reconstruct the electrical impedance distribution. Results show that the proposed method can achieve the expected imaging effect. Use of the VMD method to process the multi-frequency signal data is more accurate and gives a better imaging effect than previous methods. The proposed method can be applied to multi-frequency electrical impedance imaging in practice.

KEYWORDS: Electrical impedance tomography, multi-frequency EIT, variational mode decomposition, digital quadrature demodulation, plant root zone.

1. Introduction

The main function of a plant's root zone is to absorb water and nutrients. The complete root zone of a plant includes both the root system and the soil, and the soil provides the water and nutrients necessary for growth of the root system. Therefore, monitoring of dynamic changes in the root zone is very helpful in efforts to increase crop yields, especially in arid areas. Electrical impedance tomography (EIT) is used to measure electrical conductivity (resistivity) distributions. The array electrode that is placed on the surface of the object to be tested is used to inject a specific excitation current into the object. Using the corresponding measured surface voltage information, an image of the impedance distribution and its changes within the measured domain can then be reconstructed. EIT is a nondestructive imaging method. The EIT system required is small in size, low in cost, and does not require a strictly controlled working environment; the system can perform measurements multiple times and can be used repeatedly, which means that it has very broad application prospects in numerous fields [15].

In 1983, Barber and Brown of the University of Sheffield in the UK proposed the applied potential tomography imaging technique, which laid a solid foundation for the future development of EIT [1]. Barber and Brown then led the research team that developed the Sheffield Mark I EIT system [4]. In 1995, the same research team upgraded the Mark I EIT system and developed the Mark II EIT real-time data acquisition system for use in clinical medicine [17]. Since then,

researchers in the USA and the UK have successively developed EIT imaging systems for breast cancer detection and heart failure monitoring applications that have made major contributions to biomedicine. In 2016, a low-cost and portable EIT imaging system was also developed for cancer detection [29]. In 2018, Witkowaska-Wrobel et al. applied EIT to an animal model of epilepsy to prove that the onset and location of epilepsy are both predictable; their work had important guiding significance for preoperative evaluation of human epilepsy patients [36]. In 2019, Hannan et al. reconstructed images of the impedance changes caused by the rapid electrical activity that occurs during depolarization of imaging neurons, providing an approach that can improve judgment of the location of onset of certain diseases. This discovery is likely to contribute greatly to the development of clinical and in vivo EIT methods [12]. In 2019, Barrett et al. applied EIT technology to evaluation of the work of breathing performed by patients with chronic obstructive pulmonary disease (COPD) who were suffering acute exacerbations. During the evaluation process, this technique was of considerable help in the treatment of COPD, and the pain of the patients was reduced greatly [3]. In 2020, Inany et al. used EIT to acquire images safely and effectively for analysis of the connection between the distribution of ventilation methods and the levels of oxygenation damage occurring in critically ill children [13]. In 2021, Moon et al. used EIT to predict the dynamic changes in lung

ventilation occurring during spontaneous breath tests in patients with diaphragmatic dysfunction [21]. Additionally, in 2021, Redi et al. performed a simulation study to investigate the feasibility of use of EIT as a low-cost, non-invasive technology for hyperthermia treatment monitoring and assessed the method's adaptability [27].

Early EIT was a single-frequency imaging process, i.e., a single signal frequency was used as the excitation signal. Although this imaging mode required a simple hardware structure, it could only display the impedance and carry limited information at a specific frequency. Since then, multi-frequency EIT (MFEIT) technology has emerged. To acquire the electrical impedance information of the measurement object more accurately and more comprehensively, and also to make the imaging effect more accurate, a time-sharing multi-frequency EIT method known as frequency-sweep [30] EIT was proposed [40]. This imaging method was able to reconstruct the impedance distribution at several frequencies and thus obtained more information. However, a great deal of time is required to perform this process by frequency sweeping. As a result, the measured organism may change considerably during the measurement process, which may then cause unacceptable error levels in the final imaging results. To enable accurate imaging and reduce these errors, the multi-frequency simultaneous (MFS) method, i.e., mixed-frequency EIT, was proposed [11]. By using mixed signals superimposed on multiple frequencies to perform excitation and then separating the measured mixed signals, the electrical impedance information can be obtained at different frequencies simultaneously. After demodulation, the amplitude and phase information required for imaging can then be obtained. In 2007, an EIT system called KHU Mark 1 was used to perform imaging of the human brain and could provide excitation within the frequency range from 10 Hz to 500 kHz [23]. The authors then upgraded their previous system to develop the KHU Mark 2, which was a completely parallel multi-frequency EIT system. Although the Mark 2 system structure was more flexible and its data acquisition speed was faster than that of the first generation system, it was still unable to achieve long-term real-time monitoring of the electrical impedance imaging process, i.e., it could only present the electrical

impedance distribution at a specific point [22]. In 2016, Jehl and Holder added a conductivity Jacobian matrix for electrode movement to the EIT algorithm, and verified that the resulting algorithm could be used in multi-frequency EIT for electrode model correction; in addition, they realized the use of EIT technology to distinguish hemorrhagic disease from ischemic stroke [19]. In 2017, Weigand and Kemna integrated the spatial analysis capabilities of the multi-frequency EIT technique with the diagnostic potential of electrical impedance spectroscopy. Use of a swept multi-frequency EIT approach to characterize and monitor crop root systems has considerable potential for various root structure and functional imaging applications [35]. In 2018, Santos et al. demonstrated that multi-frequency EIT can be used to monitor, discover, and distinguish pathologies related to acute respiratory distress syndrome (ARDS) [31]. Because of the rapid evolution of the flow models used in high-pressure and high-temperature flow devices, high-speed and non-invasive imaging techniques are required. In 2019, Darnajou et al. introduced the theory of a 16-electrode simultaneous EIT system and established this system based on a field-programmable gate array. The signal was successfully received from the experimental setup at a frame rate of 1953 fps, which verified the feasibility of performing simultaneous multi-frequency excitation and measurement processes in EIT [20]. Virtual experiment procedures are important for development of new imaging hardware or new imaging algorithms for EIT research, and are essential for construction of accurate EIT models. In 2020, Gelidi et al. designed a chest conductor model for multi-frequency EIT and verified the accuracy of their model through EIT image reconstructions in virtual experiments [11]. In 2021, Ain and others successfully constructed a multi-frequency EIT system for use by biologists that included oscillators, buffers, a voltage-controlled current source, a multiplexer-demultiplexer, and a differential amplifier based on an Arduino Mega. Their system was tested successfully, producing images of conductors, insulators, and animal organs, to ensure its suitability for use in the biomedical field [1]. Multi-frequency EIT technology can resolve the problems of insufficient electrical impedance information acquisition and long measurement times, which lead to large errors, and can basi-

cally fulfil specific EIT functions in medical and other fields. The measured multi-frequency signal must be separated into independent waveform components at a given frequency for imaging. The multi-frequency EIT system must then achieve effective blind signal separation. The system design required to achieve this function is more complex than that of a single-frequency EIT system. Therefore, the development of a synchronous multi-frequency EIT system that can realize the required function and output an accurately separated multi-frequency measurement signal can promote the development of EIT technology overall, and will be of major significance for all fields that require application of EIT technology. The purpose of the work in this paper is to study the acquisition, separation, and processing of the detection signal in the multi-frequency EIT system, and to ultimately realize simultaneous multi-frequency EIT imaging of the plant root zone. The main innovation proposed in this paper is application of the variational mode decomposition (VMD) algorithm to the EIT system. The VMD algorithm can enable rapid imaging of the root zone and obtain the results at multiple frequencies simultaneously. The contributions made by the work in this article are as follows. The VMD algorithm separates measured multi-frequency signals and obtains their amplitude and phase information before imaging, thus realizing high-speed multi-frequency imaging. In addition, the separation process of the digital orthogonal separation algorithm was also studied in this research and the method was applied to EIT signal processing. Finally, the separation effects and the final imaging results obtained from the VMD algorithm and the digital orthogonal separation algorithm were compared. The results prove that VMD offers more advantages in terms of signal decomposition.

2. Related Works

The signals that are acquired or generated in real life are not often simple single-frequency signals; usually, a signal is composed of multiple single-frequency signals that are superimposed upon or even coupled to each other. In many cases, these mixed signals cannot be processed directly. It is then necessary to perform blind signal separation of the mixed signal first, and subsequently process the multiple separated signal components using a single-frequency signal processing flow. To ensure the validity and accuracy of the results obtained, it is necessary to find an algorithm that can separate the mixed signals accurately. As early as the 1980s, Herault and Jutten proposed a new algorithm for this purpose. This algorithm could separate independent source signals successfully in the linear mixed model; this work represents the beginning of blind signal separation (BSS) theory [14]. BSS is the process applied when the characteristics of the source signal and the transmission channel are unknown and the source signal components are output from a known sensor. Since then, researchers have gradually developed the BSS algorithm further, and have constantly improved the theory and the application method. In 2017, Langkam and Deb proposed a double estimation method for use in BSS. This method can estimate the state and parameters of the dynamic system simultaneously when there are only noisy data available. The method adopted the framework of the dual extended Kalman filter, in which two independent filters run at the same time, to achieve basic signal separation [16]. Because of the large numbers of calculations required and the slow calculation speed of the time-domain algorithm, Wang et al. converted the time-domain convolution operation into a frequency-domain product operation in 2017. This change improved the efficiency of BSS algorithms [33]. In 2018, Oliveira et al. proposed the use of multi-resolution analysis in the three resolution ranks of the wavelet transform, and then separated the source signal using the AMUSE algorithm with different resolution ranks. The results were better than those obtained when using the original AMUSE method alone to estimate the signal [24]. In 2019, Chua and Klejin proposed a low-delay method for BSS. Because the long analysis window used in the traditional method will involve a long calculation delay, it cannot be used in real-time systems. However, the method proposed by Chua and Klejin reduced the calculation delay while also retaining good separation properties [6]. In 2020, Lu et al. proposed an online BSS method with an adaptive step size based on an isometric adaptive separation method to find a valid equilibrium between the convergence rate

and the steady-state error of online BSS; this method demonstrated high estimation precision [18]. In 2021, because the vibration signal of the composite fault of a rotary mechanical machine acquired in the field had a complex noise source, Feng et al. addressed this problem by proposing a wavelet package analysis and fast independent component analysis extraction method for the source fault signal [9]. As the research progress discussed above indicates, various methods for signal separation have been proposed, and later generations of researchers have improved the BSS algorithm on the basis of the previous studies. This has made the BSS algorithm increasingly accurate and it is thus being gradually applied to the speech recognition and mechanical failure analysis fields.

The VMD algorithm is a BSS method that was proposed by Dragomiretskiy and Zosso in 2014. This algorithm can decompose and estimate the signal, and can determine the center frequency of each component of the signal by searching iteratively for the optimal solution to the variational model during the process of acquisition of the decomposed components, thus realizing effective separation of each of the signal components adaptively [7]. In 2017, An et al. proposed a gear malfunction diagnosis method based on the VMD algorithm. Their method used VMD to decompose complex multi-frequency signals into several simple components and analyzed the signal components obtained through an envelope demodulation process; the method can be applied effectively to gear malfunction diagnosis [28]. In 2018, Yadav et al. proposed a speech parameterization method for automatic speech recognition based on the VMD algorithm. The researchers used VMD to decompose the short-term amplitude spectrum that they had acquired into several components and then smoothed them. The front-end acoustic function that was obtained after the final processing step showed increased resistance to both environmental noise and pitch changes [37]. In 2019, Pandey and Seeja used VMD as a characteristic collection technology and a deep neural network as a classifier to propose a topic-independent emotion identification technology for electroencephalography (EEG) signals. This technology can identify the common EEG patterns that have nothing to do with specific emotions or with the individual. When compared with the traditional technology level available at that time, this combined VMD and deep neural network technology performed better in emotion recognition applications where the EEG signals are independent of specific objects [25]. In 2020, Zhang et al. used the VMD algorithm to decompose a source signal into a given number of components K. These components were then arranged in descending order of frequency. After the feature mode matrix was constructed, the microseismic signals and blasting vibration signals in the source signals could be distinguished, i.e., the method could identify microseismic events accurately [39]. In 2021, Kaur et al. used VMD to decompose a signal into several components during the process of suppression of the noise in an EEG signal of depression. They then used the discrete wavelet transform and the wavelet packet transform to reduce the noise of the artificial components, rather than use detrended fluctuation analysis as the basis of a mode to shield these artificial components entirely. Background artifact pollution reduces the effectiveness of almost all neural engineering applications based on EEG. However, use of this artifact removal system in combination with VMD technology can provide clinicians with a good processing method that can help to avoid delays in the signal diagnosis of depression [5]. The research discussed above shows that since the VMD algorithm was initially proposed, it has been improved continuously and has been applied to fields including industry, nature, and medicine. The above also provides feasible indications of ways to apply the VMD algorithm to agricultural EIT research in this study.

3. Methods

The principle of the approach in this research is to use a synthetic signal produced by superimposing sine waves at multiple frequencies to act as an excitation signal to excite the measurement electrodes. The multi-frequency measurement signals are then collected, and the measured signals are separated using the VMD method. Finally, the amplitude and phase are extracted for each signal component and the signal is then imaged. The experimental process is illustrated in Figure 1.

Figure 1
Experimental process
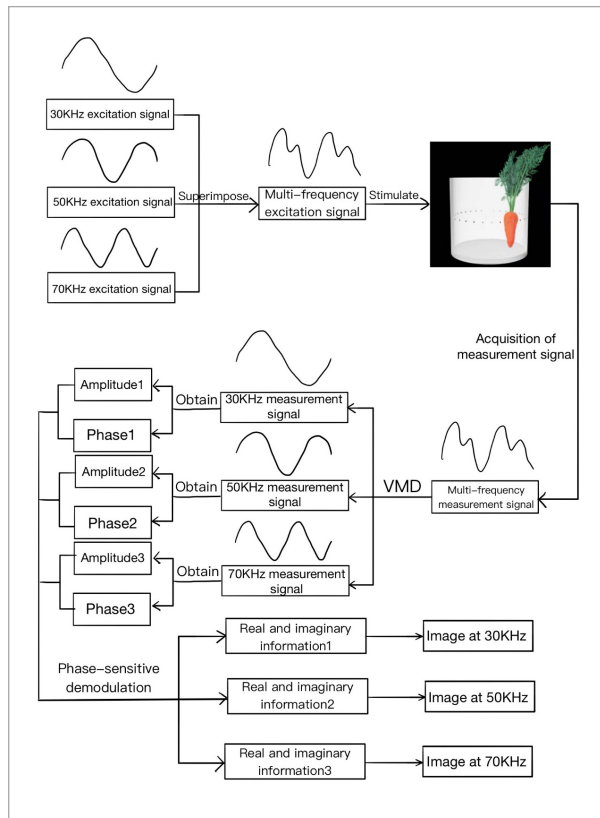
3.1. Experimental Environment and Data Acquisition

In this study, a 32-electrode EIT device was used. The overall system hardware structure includes sinusoidal signal generators, voltage-controlled current sources, channel switching circuits, electrodes, signal amplifiers, analog demodulation, filtering, and analog-to-digital (A/D) signal acquisition modules. A digital synthesis chip is used to generate a sine signal. A voltage-controlled current source then converts the sinusoidal signal into an excitation signal, and injects this signal sequentially into the measurement container through the channel selection circuit. The measurement circuit uses a serial design. The measurement signal is amplified differentially using the preamplifier and is then input into a demodulation circuit composed of a multiplier and a low-pass filter.

The demodulated signal is subsequently collected by the A/D module, and the collected voltage value is finally sent to the upper computer through the RS485 bus communication protocol. The control signal in this circuit is then transmitted by the single-chip microcomputer after it receives the required command from the upper computer to ensure the correct time difference between the excitation and measurement processes. The hardware design structure of this system is illustrated in Figure 2.

Figure 2
EIT system structure
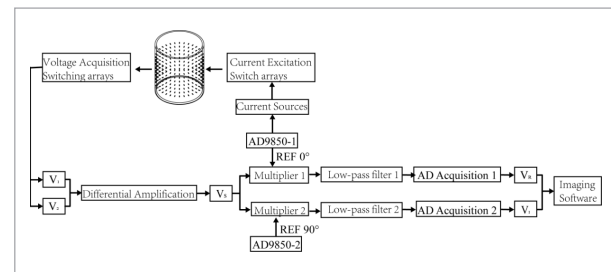
The electrode conductivity used in the simulation is 4.032×10^6 S/m. The conductivity of the internal cylindrical medium is 2 S/m, and its relative permittivity is 5. The parameters of plexiglass are used for the periphery, where the conductivity is zero and the relative permittivity is 3.7. In the experiment, uniform salt water was used as the test medium, and plant tissue (carrot) was used as the test object. The carrot had a diameter of 69 mm and a height of 120 mm; it was located on the line of electrode nos. 1 and 17, and its center was located 92.5 mm away from the center of the generic plexiglass barrel. In accordance with a previous method used to obtain sensitive frequencies [32] and the growth conditions of the soil and the crops of interest [34], we set signals with frequencies of 30 kHz, 50 kHz, and 70 kHz to excite the pure salt water medium and the medium containing the measured object, where the excitation current was 8 mAp-p. A carrot was selected as the object to be tested in the experiment because the boundary voltage needs to vary by a specific level to verify the imaging capabilities of the system; the use of a larger biological object for testing can ensure that the boundary

voltage will change sufficiently. The carrot, as a large biological object, can thus ensure that the change in the boundary voltage is large enough.

The EIT system contains 32 electrodes in each layer, and uses adjacent excitation and adjacent measurement methods for signal excitation and acquisition, respectively. As shown in Figure 3, electrode No. 1 was excited, and all other electrodes with the exception of electrode No. 1 were measuring electrodes. The voltages between pairs of adjacent measuring electrodes were measured from electrode No. 2 up to electrode No. 32. This means that when electrode no. 1 was excited, a total of 29 sets of voltage values between electrode No. 2 and No. 3, No. 3 and No. 4, ..., and No. 31 and No. 32 were measured. Similarly, when measuring electrode No. i, then the voltages between electrode No. i+1, No. i+2, No. i+3..., were measured. A total of 32×29=928 measurements were thus required.

Figure 3
Electrode diagram
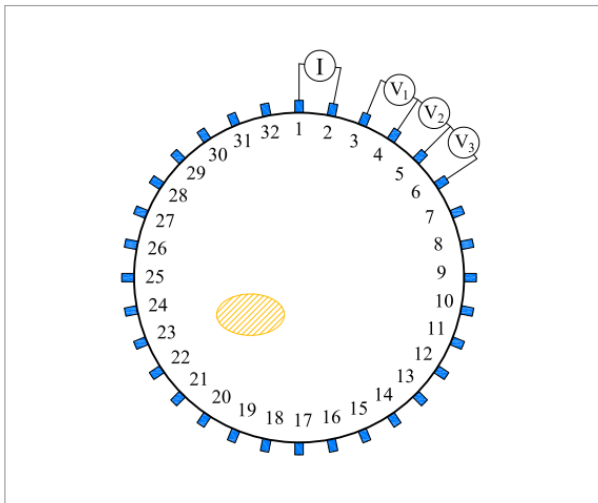
After the system was powered on, the control board closed all channels by default. First, the measurement system had to be connected through the serial port to set both the serial port number and the baud rate. Then, the excitation parameters were set; this mainly involved setting the frequency and amplitude of the excitation signal and the control board number. Finally, the incentive mode was selected. After all settings were completed, the measurement process

commenced, and data were saved for each excitation position that was measured. The saved data were the original A/D signal measurement data, and these A/D signal data represented the average values from eight measurements. There were two data in each group. Here, the 16-bit A/D converter (ADC) used the standard internal voltage of 2.4 V. After conversion, the two measured values become voltage values, they respectively represent the 90° reference voltage value $V_I(t)$ and the 0° reference voltage value $V_R(t)$. The equations for calculation of the signal phase and amplitude, represented by φ and A_s, respectively, are given as follows:

$$\varphi = \arctan\left(\frac{V_I A_{ref}}{V_R A_{ref\,90}}\right), \tag{1}$$

$$A_s = 2\sqrt{\left(\frac{V_I}{A_{ref\,90}}\right)^2 + \left(\frac{V_R}{A_{ref}}\right)^2}, \tag{2}$$

where the amplitudes A_{ref} and A_{ref90} were known, and from which 928 groups of amplitudes and phases can be obtained. The three Excel spreadsheet correspond to the frequencies of 30 kHz, 50 kHz, and 70 kHz, respectively. Because the frequency, amplitude, and phase parameters were all known, a sinusoidal waveform given by $V(t) = A\sin(\omega t + \varphi)$ can then be determined. The multi-frequency signal can thus simulate the multi-frequency measurement signals that were collected directly from the experimental device under the multi-frequency excitation conditions.

3.2. Multi-Frequency Signal Separation

Because the excitation signal is a multi-frequency-superimposed signal, the measured signal thus also contains multiple frequencies. Therefore, it is necessary to decompose this multi-frequency measurement signal, separate it into multiple single-frequency signals, and then image them separately. In this way, the amplitude and phase information at multiple frequencies can be obtained at the same time, thereby greatly improving the imaging speed. This paper used the VMD method to separate the multi-frequency signals, then also used the digital orthogonal decomposition method to separate the same measurement signals, and finally compared the separation processes and imaging effects of the two decomposition methods.

3.2.1. Variational Mode Decomposition (VMD) Method

The VMD algorithm [8] was used in this work for decomposition of the collected multi-frequency measurement signals. This algorithm can decompose a multi-frequency signal into multiple single-frequency signals. The principle of the algorithm is to find the optimal solution for the variational model through an iterative process, enabling calculation of the center frequency and bandwidth for each component, and finally realizing frequency domain division of the signal and effective separation of each of the components.

The basis function can be obtained by using the VMD algorithm, i.e., the update formula for each signal component, which is expressed as

$$\hat{u}_{\hbar}(\omega) = \frac{\hat{f}(\omega) - \sum_{i \neq \hbar} \hat{u}_i(\omega) + \frac{\hat{\lambda}(\omega)}{2}}{1 + \alpha(\omega - \omega_{\hbar})^2}, \tag{3}$$

where $\hat{u}_{\hbar}(\omega)$ represents the basis function obtained by decomposition, i.e., the single-frequency signal component. Here, $\hat{f}(\omega)$ is the representation of the signal to be separated in the frequency domain, where $\hat{\lambda}$ is updated using the gradient descent method as follows:

$$\hat{\lambda}^{n+1}(\omega) = \hat{\lambda}^{n}(\omega) - \tau\left(\hat{f}(\omega) - \sum_{\hbar} \hat{u}_{\hbar}(\omega)\right), \tag{4}$$

where $\omega_{\hbar}$ is the center frequency of each signal component. The update formula for the center frequency is

$$\omega_{\hbar} = \frac{\int_0^{\infty} \omega \left|\hat{u}_{\hbar}(\omega)\right|^2 d\omega}{\int_0^{\infty} \left|\hat{u}_{\hbar}(\omega)\right|^2 d\omega}. \tag{5}$$

After the amplitude and phase information is obtained from the separated single-frequency signal, imaging can then be performed.

Because the measurement table has 29 rows and 32×2 columns, it is difficult to process. Therefore, the table is first changed into a 928×2 format, where each row represents the amplitude and phase of a single waveform. Then, after the waveforms corresponding to the number of rows in the table under the three excitation frequencies were added, 928 multi-frequency waveforms were obtained.

After the input parameters were set, the VMD function was used to separate the 928 multi-frequency signals. After the VMD separation process, 928×3 · $\hat{u}_{\hbar}(\omega)$, i.e., the separated single-frequency signal, was obtained. First, $\hat{u}_{\hbar}(\omega)$ was decomposed into a DC component and a group of sine waves with different amplitudes, frequencies, and phases using a Fourier transform approach. Because the frequency was known, the sine wave could be described fully using the two characteristic amplitude and phase values at this time. Although the amplitudes and phases of all sampled signals could be obtained, the signal components that were decomposed by the VMD method were not necessarily arranged in order of frequency. Therefore, it was also necessary to add a sorting statement to sort the signal components by frequency, and the obtained amplitudes and phases were then divided into the table under each frequency according to the frequency used for imaging.

3.2.2. Digital Orthogonal Decomposition Method

For comparison, the number of samples in a period was set to be the least common multiple of the number of samples in a period for each frequency component during the parameter setting process, and the orthogonal decomposition function was then used directly to separate the 928 multi-frequency signals.

The sampling result for a signal with K frequency components is given by:

$$S(\mathrm{n}) = \sum_{\hbar=1}^{p} A_{\hbar} Sin\left(\frac{2\pi}{N_{\hbar}} n + \varphi_{\hbar}\right), \tag{6}$$

where $A_{\hbar}$ represents the amplitude of the $\hbar$ th frequency component. In addition, $\varphi_{\hbar}$ represents the phase of the $\hbar$ th frequency component. $N_{\hbar}$ represents the number of samples of the $\hbar$ th frequency component in a period. N_c is taken to be the least common multiple of $N_1, N_2, N_3, ..., N_K$, and then, according to the quadrature demodulation formula:

$$\begin{cases} (I_{\hbar}, Q_{\hbar}) = \frac{1}{N_{\hbar}} \sum_{n=0}^{N_c - 1} S(n) \cdot e^{j\frac{2\pi n}{N_{\hbar}}}, \\ \hbar = 1, 2, ..., K, \end{cases} \tag{7}$$

where $I_{\hbar}$ is the real part of the $\hbar$ th frequency component sampling result $S(n)$. $Q_{\hbar}$ is the imaginary part of the $\hbar$ th frequency component sampling result $S(n)$.

When the real and imaginary components are known, the amplitude and phase of each frequency component can be found as follows.

$$\begin{cases} A_\hbar = \sqrt{I_\hbar^2 + Q_\hbar^2}, \\ \varphi_\hbar = \arctan \dfrac{I_\hbar}{Q_\hbar}, \\ \hbar = 1, 2, \dots, K. \end{cases} \tag{8}$$

After separation was performed using this algorithm, the amplitude and phase information of the 928×3 single-frequency signals could be obtained directly. After the amplitude and phase data were classified according to their frequencies, they were then summarized in a table using the imaging data format of the Electrical Impedance and Diffuse Optical Tomography Reconstruction Software (EIDORS), and they were then suitable for use in imaging applications.

3.3. Imaging

In this study, the open-source software package EIDORS 3.10 was used for imaging analysis of the measured voltage data. EIDORS is an open-source software suite for use in EIT and diffuse optical tomography (DOT) image reconstruction. The software is used specifically to model and solve forward and inverse problems. EIDORS contains four main elements: the data, the image, the forward problem model, and the inverse problem model. The data are obtained from each measuring electrode after each excitation. The image is then reconstructed by processing the measured data. The forward problem must first be divided into a finite element method (FEM) model of the measurement domain, and then the size, position, and excitation mode (current excitation/voltage acquisition mode) should be set for each electrode; finally, the function for solution of the forward problem model, the contact impedance, the solver, and the Jacobian parameters should all be set. The inverse problem model includes all information required to perform imaging, and its data contain the model of the forward problem. The parameters that must be set in the inverse problem include the solver, the hyper parameters, the Jacobian parameters, and the reconstruction method (time difference imaging).

The imaging steps involved in the process of electrical impedance imaging of carrots are specified in Figure 4.

Figure 4
Imaging steps
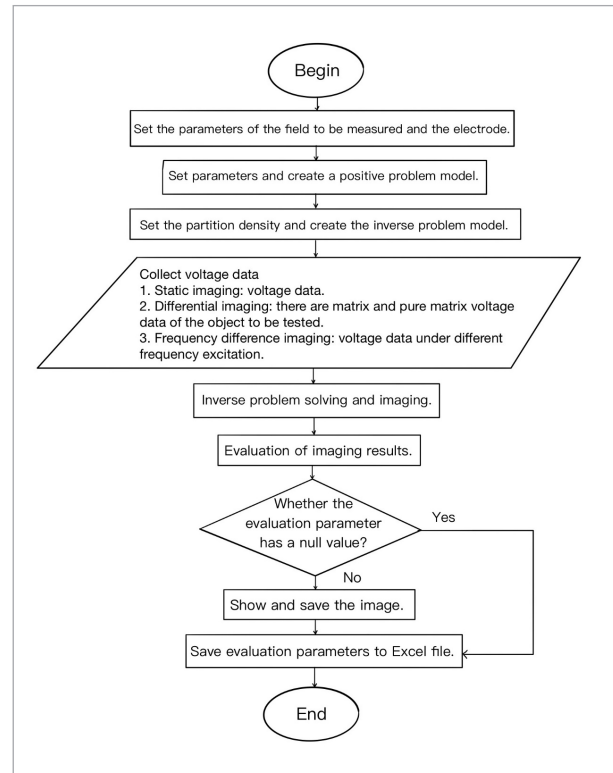
4. Results

4.1. Simulation Experiment

In the simulation experiment, a circular target with a radius of 10 mm was placed within the field to be measured. The target conductivity was 2 S/m, the background conductivity was 1 S/m, the number of electrodes was 32, and the excitation mode used was adjacent excitation. By modifying the electrical conductivity values to be 2 S/m, 3 S/m, and 4 S/m, three data sets were obtained and were simulated as the measured data at three frequencies. Each single-frequency signal was determined by using the simulated amplitude and phase data, and these signals were then superimposed. The superimposed multi-frequency signal was then separated using both the VMD method and the digital orthogonal decomposition algorithm. The separated signals were classified and imaged based on their corresponding frequencies. Here,

the imaging results for the real and imaginary components of the amplitude obtained by the VMD method and the digital orthogonal decomposition method were compared with the original imaging results obtained under single-frequency excitation. Among these results, the imaging process for the real part is resistance imaging, which reflects the nonbiological tissues. The imaging process for the imaginary part is reactance imaging, which reflects the biological tissues. Amplitude imaging has the characteristic that it can be used for imaging of both the real and imaginary components, but the amplitude is a single value without a phase angle, which means that the complex impedance should be used.

As shown in Table 1, the amplitude image determined from the original data was compared with the images obtained from the data when processed using the VMD method and the digital orthogonal decomposition method. The units of the imitated color bar are S/m.

Table 1
Amplitude imaging results comparison

	Original	VMD	Digital orthogonality
30 kHz			
50 kHz			
70 kHz			

As shown in Table 2, the real component image from the original data was compared with the corresponding images obtained from the data processed using the VMD method and the digital orthogonal decomposition method. The units for the imitated color bar are S/m.

As shown in Table 3, the imaginary component image from the original data was also compared with the corresponding images obtained from the data processed using the VMD method and the digital orthogonal decomposition method. The units for the imitated color bar are S/m.

Comparison of the imaging results in the three tables shows that the images formed using the simulation data at the three frequencies when separated using the VMD method and the digital orthogonal decomposition method were almost the same as those from the imaging results of the single-frequency simulation. However, comparison of the subtle differences in image color and position showed that the VMD image was closer to the original image. The results show that these two methods can both perform BSS very well and that they ultimately completed the imaging tasks, but the VMD method showed a slightly better effect.

The following five evaluation indicators were used in this study.

The amplitude response (AR) is used to represent the ratio of the pixel amplitude in the image to be measured to the pixel amplitude in the reconstructed im-
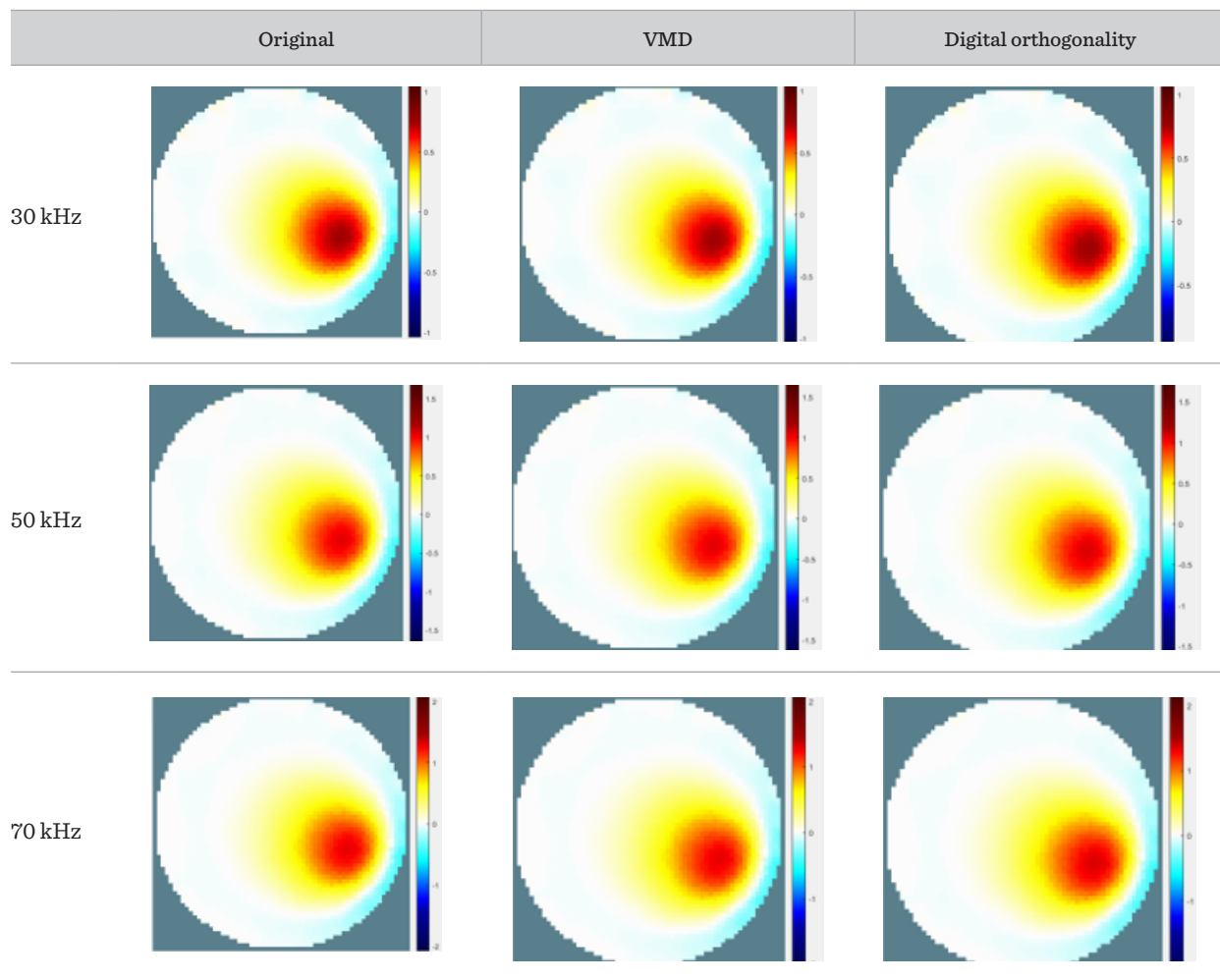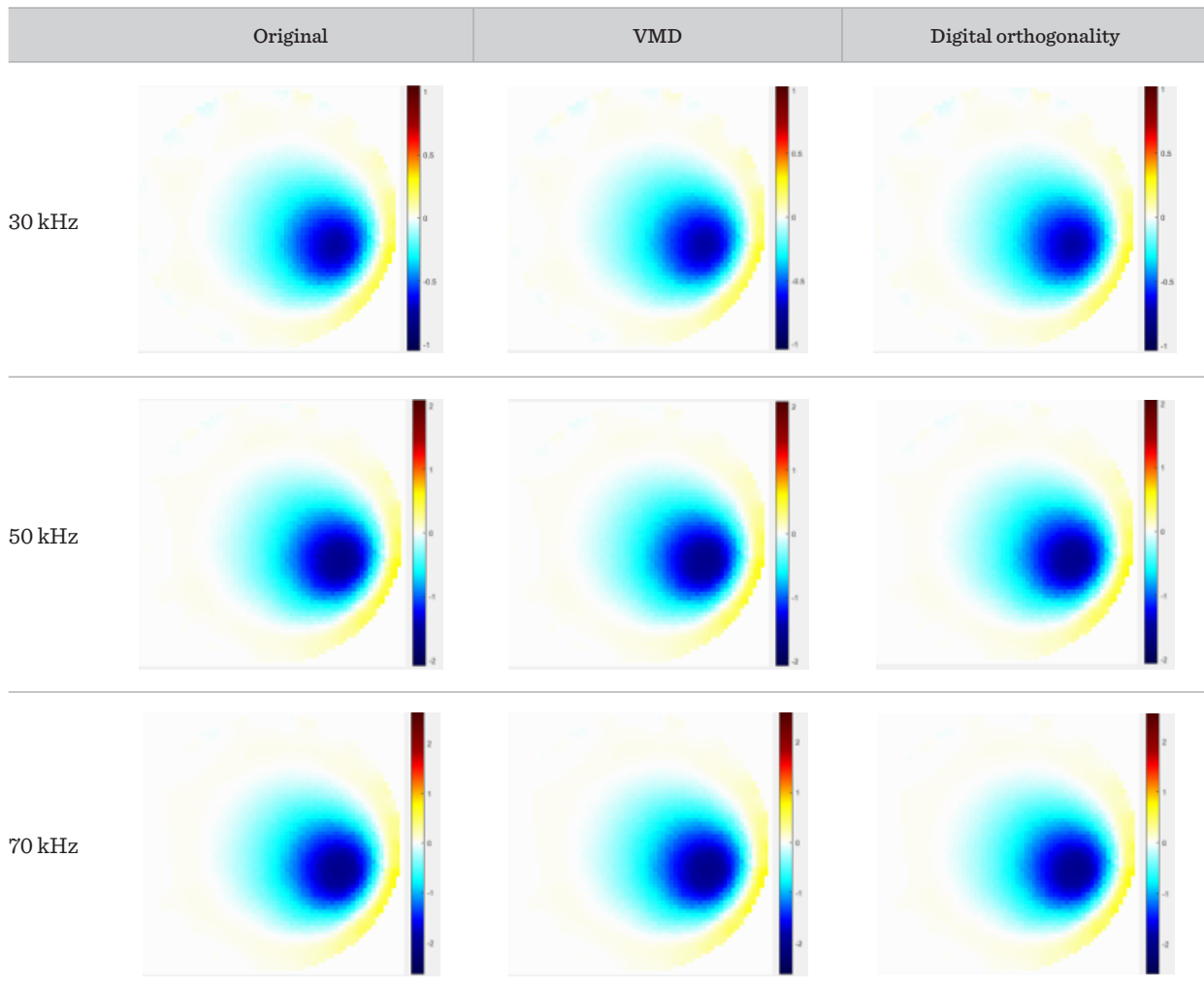
Table 2

Real part imaging results comparison

Table 3

Imaginary part imaging results comparison

	Original	VMD	Digital orthogonality
30 kHz			
50 kHz			
70 kHz			

age. A smaller change in AR indicates a better reconstruction effect.

The position error (PE) is used to reflect the deviation of the reconstructed image position relative to the actual position of the object to be measured. A smaller and more stable parameter value in this case indicates a better reconstruction effect.

The resolution (RES) is used to measure the size of the reconstructed image of the object to be measured as a part of the area to be measured. A more uniform and smaller resolution means that the shape of the conductivity distribution of the object to be measured can be represented more accurately.

The shape deformation (SD) is a proportional parameter. When the object to be measured is close to the edge of the area to be measured, strange deformation artifacts will then appear. The SD is used to measure the proportion of the quarter amplitude group that cannot match a circle with the same area. A more uniform and smaller value indicates a better reconstruction effect in this case.

The ring (RNG) indicates whether or not the area with opposite signs surrounding the main area to be measured can be displayed in the reconstructed image. A more uniform and smaller RNG value indicates a better reconstruction effect.

In the simulation experiment, the evaluation indexes of the original single-frequency imaging process and the imaging processes after the separation of the two methods were obtained. Tables 4-6 contain the values of the AR, PE, RES, SD, and RNG that were obtained under 30 kHz, 50 kHz, and 70 kHz excitation, respectively, for single-frequency excitation imaging and for imaging after separation by the VMD method and the digital orthogonal decomposition method. These five indicators were then compared.

Comparison of the five evaluation indicators from the simulation experiment results presented in the Tables 4-6 above shows that four of the indicators, i.e., PE, RES, SD, and RNG, were completely consistent. However, the AR from the VMD method was smaller at all three frequencies. It is thus obvious that the ratio of the pixel amplitude of the original image to that of the reconstructed image is small, and the imaging error is thus small.

Table 4

Comparison of evaluation indexes for each method at 30 kHz

30 kHz	Original	VMD	Digital orthogonality
AR	578.18149	576.29715	578.21823
PE	58.75239	58.75239	58.75239
RES	0.45960	0.45960	0.45960
SD	0.03058	0.03058	0.03058
RNG	0.13747	0.13747	0.13747

Table 5

Comparison of evaluation indexes for each method at 50 kHz

50 kHz	Original	VMD	Digital orthogonality
AR	1031.21037	1026.01406	1031.20386
PE	58.56205	58.56205	58.56205
RES	0.45960	0.45960	0.45960
SD	0.03211	0.03211	0.03211
RNG	0.13291	0.13291	0.13291

Table 6

Comparison of evaluation indexes for each method at 70 kHz

70 kHz	Original	VMD	Digital orthogonality
AR	1296.22918	1289.67802	1296.10275
PE	58.57162	58.57162	58.57162
RES	0.46031	0.46031	0.46031
SD	0.03048	0.03048	0.03048
RNG	0.13175	0.13175	0.13175

In conclusion, in the simulation experiments, the VMD algorithm was able to realize accurate separation of the multi-frequency measurement signals completely. The process accuracy was high, and better imaging results can thus be obtained using this algorithm. These results were reproducible and the imaging remained stable. The VMD algorithm can complete the imaging process at more than three frequencies within the single-frequency excitation process time to obtain a frequency image. Use of this algorithm shortened the imaging time greatly and improved the imaging efficiency. Comparison with the digital orthogonal decomposition method shows that in the high-frequency excitation case, the digital orthogonal decomposition method required an increased number of sampling points, which took a longer time to process. Additionally, its separation effect was worse than that of the VMD algorithm, and the final imaging result was not as accurate as that obtained when using the VMD method. The VMD method was also relatively stable at high frequencies.

4.2. Actual Measurement Experiment

In the experiment, a potassium chloride solution with a concentration of 2.012 mM was used as the measurement medium. A conductivity meter (DDSJ-308A, Inesa Instrument, China) was used to measure the background conductivity. The conductivity of the pure brine was 227 µS/cm.

Plant tissue (carrot tissue) was used as the object to be measured in the experiment. The carrot used had a diameter of 69 mm and a height of 120 mm. The carrot was located near electrode nos. 16 and 17, and its circular center was located 92.5 mm from the center of the plexiglass barrel. Signals at 30 kHz, 50 kHz, and 70 kHz were used to measure the pure saline medium and the medium that contained the substance to be measured. The experimental system is shown in Figure 5.

The data measured under excitation were used to perform imaging, and the results of amplitude imaging, real part imaging, and imaginary part imaging for single-frequency excitation were obtained. Then, the data measured for the three frequencies were sorted out and superimposed. The VMD method and the digital orthogonal decomposition method were then used to decompose the superimposed original data, and the imaging results obtained after decomposition by these two methods were compared with the results

Figure 5

Carrots are located near electrode No. 16 and No. 17 at a distance of approximately 1 cm in a plexiglass tube containing a pure KCl solution with conductivity of 227 µS/cm

of direct imaging using the original data. The images that were compared included the amplitude, real part, and imaginary part imaging results.

As shown in Table 7, the amplitude image from the original data was compared with the images from the data processed using the VMD method and the digital orthogonal decomposition method. The units for the imitated color bar are S/m.

As shown in Table 8, the real part image from the original data was compared with the images from the data processed using the VMD method and the digital orthogonal decomposition method. The units for the imitated color bar are S/m.

As shown in Table 9, the imaginary part image from the original data was compared with the images from the data processed using the VMD method and the digital orthogonal decomposition method. The units for the imitated color bar are S/m.

Comparison of these three tables shows that both the VMD method and the digital orthogonal decomposition method can separate the multi-frequency signals accurately. In addition, the imaging results obtained were also very close to the single-frequency raw data imaging results. When assessed from the perspectives of the amplitude, real part, and imaginary part imaging results, there were almost no differences between the two decomposition methods. As shown

in Tables 7 and 8, the VMD separation effect in the actual measurement experiment at the appropriate frequency in a noncentral location was similar to the digital orthogonal decomposition effect.

In the actual measurement experiment, the evaluation indexes for the original single-frequency imaging method and for the imaging method after separation of the central location were obtained. Tables 10-12 present the values of the AR, PE, RES, SD, and RNG that were obtained under excitation at 30 kHz, 50 kHz, and 70 kHz, respectively, for single-frequency excitation imaging and for imaging after separation by the VMD method and the digital orthogonal decomposition method. These five indicators are then compared.Comparison of the five evaluation indicators presented in these tables shows that there were only small differences among the three indexes for the PE, RES, and SD. However, the AR and RNG values for the VMD images were much smaller. Obviously, the reconstruction effect obtained when using the VMD algorithm was slightly better, and the imaging error obtained was small.

Table 7

Amplitude imaging results comparison

Original	VMD	Digital orthogonality

30 kHz

50 kHz

70 kHz
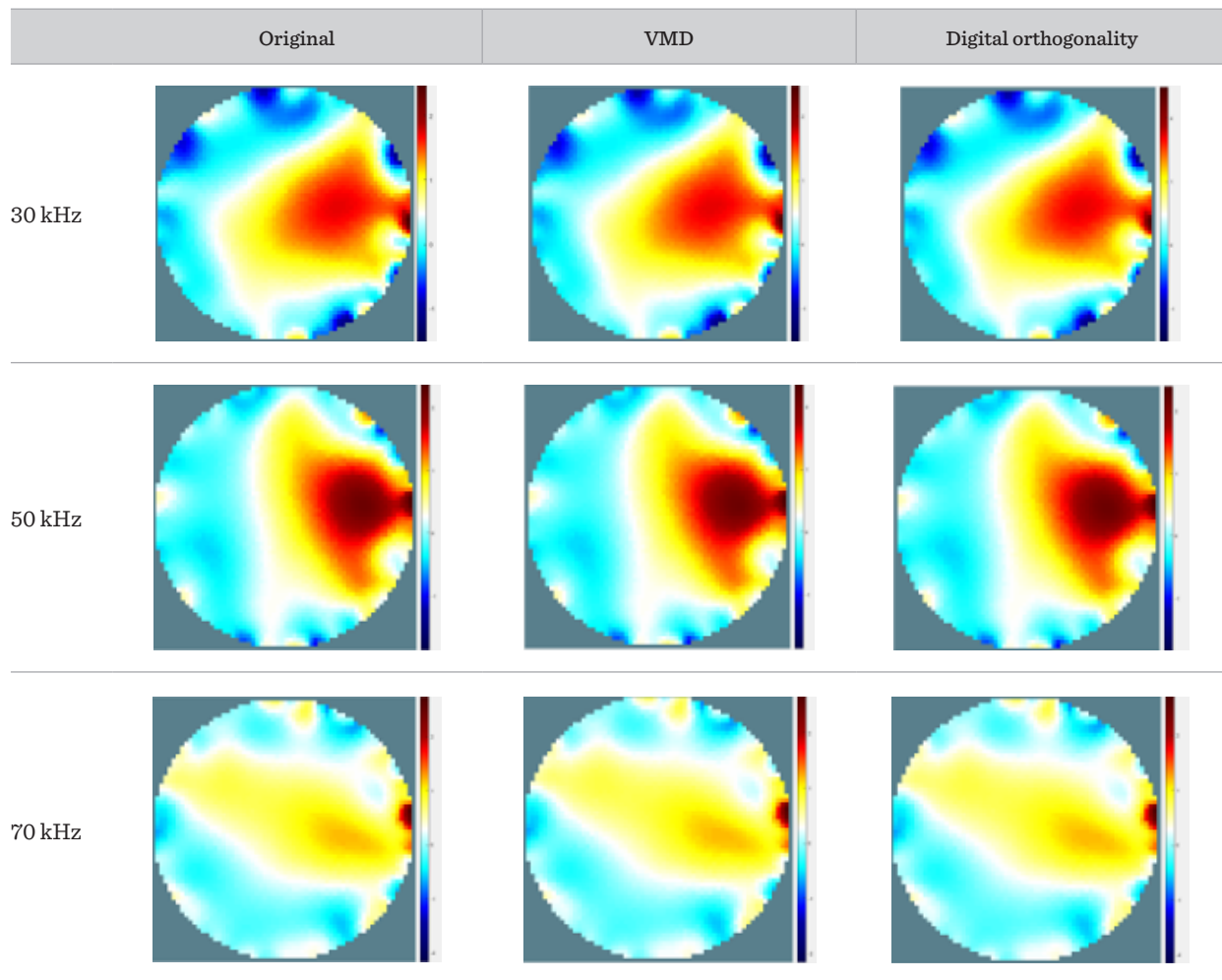
In summary, both the VMD algorithm and the digital orthogonal decomposition algorithm can satisfy the requirements for accurate separation of multi-frequency measurement signals in both simulation experiments and actual experiments, and both methods can provide good imaging effects. Both methods can complete the imaging process at three frequencies within the time required for single-frequency excitation to obtain a single-frequency image. The imaging time was greatly shortened and the imaging efficiency was greatly improved by both approaches. However, although the two methods can achieve the same goals from an imaging viewpoint, the VMD method is significantly better than the digital orthogonal decomposition method from a data accuracy viewpoint in terms of parameters such as the AR and RNG. Additionally, at higher frequencies, the effect of the orthogonal decomposition approach is better in terms of the numbers obtained, but the VMD method is faster.

Table 8
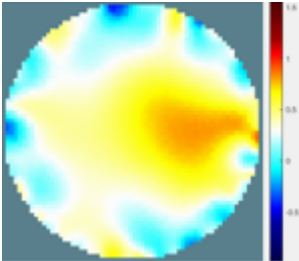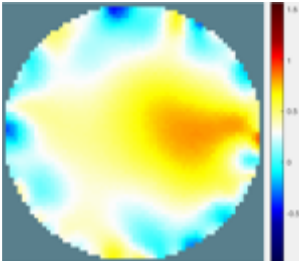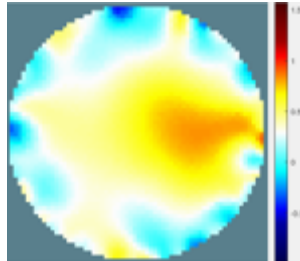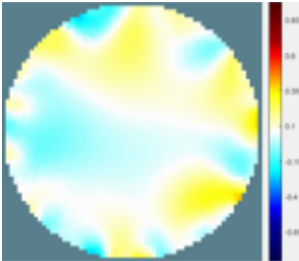
Real part imaging results comparison
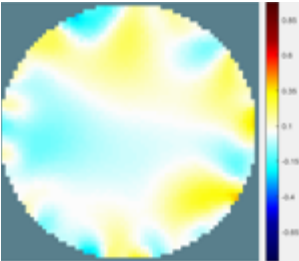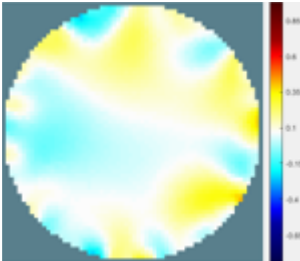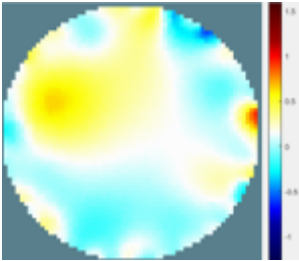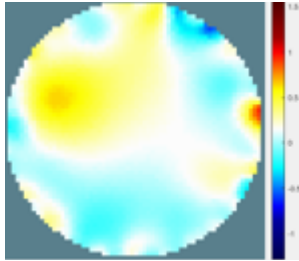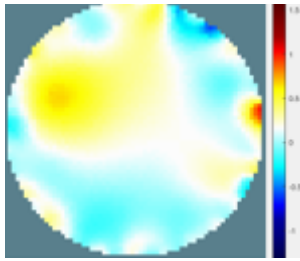
Original	VMD	Digital orthogonality

30 kHz

50 kHz

70 kHz

Table 9

Imaginary part imaging results comparison

	Original	VMD	Digital orthogonality
30 kHz			
50 kHz			
70 kHz			
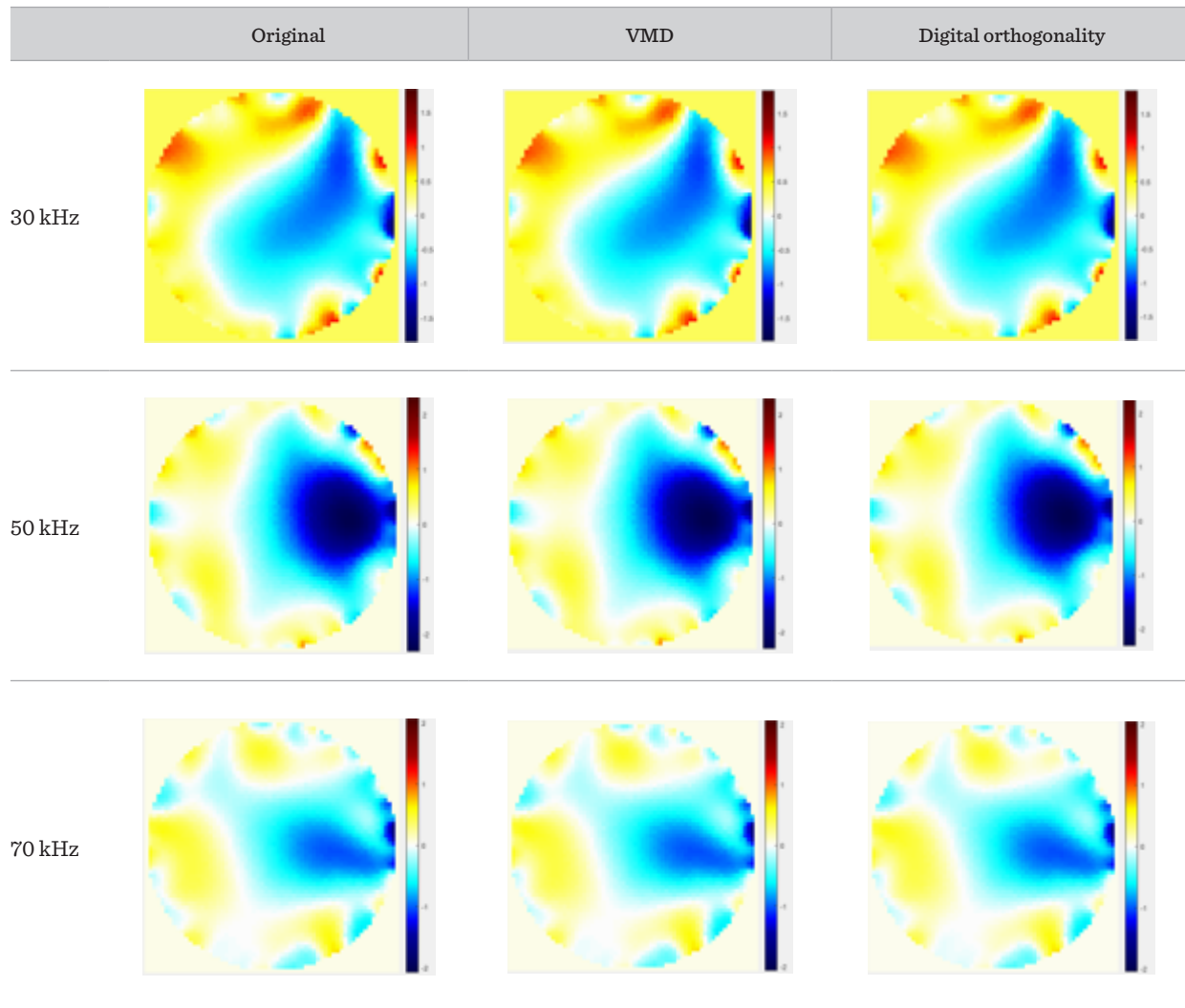
Table 10

Comparison of evaluation indexes for each method at 30 kHz

30 kHz	Original	VMD	Digital orthogonality
AR	1758.17658	1750.86668	1758.18526
PE	74.51585	74.51585	74.51585
RES	0.67485	0.67485	0.67485
SD	0.15319	0.15319	0.15319
RNG	0.07480	0.07474	0.07480

Table 11
Comparison of evaluation indexes for each method at 50 kHz

50 kHz	Original	VMD	Digital orthogonality
AR	1371.28071	1362.38903	1371.22294
PE	54.79191	54.84551	54.79191
RES	0.60119	0.60146	0.60119
SD	0.16085	0.16160	0.16085
RNG	0.14560	0.14557	0.14560

Table 12
Comparison of evaluation indexes for each method at 70 kHz

70 kHz	Original	VMD	Digital orthogonality
AR	1000.11379	996.02919	999.99052
PE	78.61844	78.67443	78.61844
RES	0.50321	0.50354	0.50321
SD	0.39158	0.39235	0.39158
RNG	0.22512	0.22463	0.22513

5. Discussion

The five evaluation criteria and the final imaging results presented above verify that the VMD method has a good decomposition effect on the three-frequency mixed signals, and the amplitude and phase errors obtained were within 0.0005. In this study, in addition to verifying that use of the VMD method is feasible, the digital orthogonal decomposition method was also used to decompose the multi-frequency measurement signals under the same conditions. Comparison of the amplitude and phase data from the two methods, along with the separated amplitude, real part, and imaginary part imaging results obtained at each given frequency, shows that the performance of the VMD method is better than that of the digital orthogonal decomposition method, which has been used widely in the multi-frequency EIT imaging field in existing paper [38].

The results indicate that the imaging performance of the VMD method is almost consistent with that of the direct imaging method under single-frequency excitation at 30 kHz, 50 kHz, and 70 kHz. In particular, when the number of mixed excitation signals is high or the excitation signal frequency is high, the advantages of the VMD method become more obvious, and the imaging effect is better.

We used the VMD method to achieve separation of synchronous multi-frequency signals and provide a more mature simultaneous multi-frequency EIT technology. We were able to acquire three or more images at different frequencies within the time taken for the single frequency EIT system to produce one image at a single frequency. The proposed approach not only greatly enhances the imaging speed, but also avoids the errors caused by the different electrical impedance distributions that occur in plants at different times.

The results verified that the VMD algorithm can extract the amplitude and phase data for each signal component at each frequency rapidly. Comparison with the original data also confirmed that the separation effect was good and that the imaging speed was extremely fast. Comparison of the amplitude imaging, real part, and imaginary part imaging results for tuberous roots, e.g., carrots, indicates that the VMD method can be applied to synchronous multi-frequency EIT in the root zones of tuberous root crops to achieve multi-frequency simultaneous rapid imaging of these zones.

Although the VMD results are very accurate, the separation speed of the method is still not fast enough to date. At present, it is only possible to generate images at multiple frequencies simultaneously, and real-time detection results cannot be guaranteed. In future research, through optimization of the VMD algorithm, we will aim to enhance the separation speed without affecting the decomposition effect. In addition, we believe that parallel computing methods can be used to improve process efficiency [26]. Therefore, it will be worthwhile to develop these approaches in our future research.

6. Conclusions and Future Work

In this paper, the VMD method was applied to the multi-frequency signal separation step in a multi-frequency EIT system for plant root zone measurement. The results of this study show that the VMD method can separate the multi-frequency measurement signal measured at the electrode effectively after a multi-frequency signal was excited. Additionally, electrical impedance images at three or more frequencies can be obtained within the time required to acquire one image in a single-frequency system, thus enabling realization of high-speed multi-frequency imaging in the root zone. In addition, this research also compared the separation effects of the VMD method and digital orthogonal decomposition on multi-frequency signals, and verified that these two methods were both effective. However, the separation effect of the VMD method was observed to be better than that of the digital orthogonal decomposition approach.

In addition to the acceleration effect of the VMD method, the experiments and optimization processes can be continued in future work to enable more accurate separation of the multi-frequency measurement signals and thus provide better imaging effects. At the same time, more excitation signals at different frequencies can be supplied to the electrodes, and electrical impedance information can be obtained simultaneously at more frequencies in a short time period.

In future work, we will expand the various data sets used in this work and improve the algorithm to increase its decomposition speed. Efforts will also be made to achieve rapid simultaneous imaging under excitation at multiple frequencies in short times, and to test the effectiveness and accuracy of the improved algorithm further. It will also be useful to expand and improve the amplitude and phase data that can be separated by the VMD method by performing experiments on different crop categories.

Acknowledgement

References

1. Ain, K, Ulum, M. F., Choridah, L, Mukhaiyar, U, Garnadi, A. D., Setyawan, N.H., et al. Design of Electrical Impedance Tomography for Biomedicine. Journal of Physics: Conference Series, 2021, 1816(1), 012043. https://doi.org/10.1088/1742-6596/1816/1/012043

2. Barber, D, Brown, B. Recent Developments in Applied Potential Tomography. APT2010.

3. Barrett, N. A., Hart, N., Camporota, L. Assessment of Work of Breathing in Patients with Acute Exacerbations of Chronic Obstructive Pulmonary Disease. COPD, 2019, 16(5-6), 418-428. https://doi.org/10.1080/15412555.2019.1681390

4. Brown, B., Seagar, A. The Sheffield Data Collection System. Clinical Physics and Physiological Measure-

ment: An Official Journal of the Hospital Physicists' Association, Deutsche Gesellschaft fur Medizinische Physik and the European Federation of Organisations for Medical Physics, 1987, 8 Suppl A. https://doi.org/10.1088/0143-0815/8/4A/012

5. Chamandeep, K., Amandeep, B., Preeti, S., Garima, J. EEG Signal Denoising Using Hybrid Approach of Variational Mode Decomposition and Wavelets for Depression. Biomedical Signal Processing and Control, 2021, 65, 102337. https://doi.org/10.1016/j.bspc.2020.102337

6. Chua, J., Kleijn, W. B. A Low Latency Approach for Blind Source Separation. IEEE/ACM Transactions on Audio, Speech and Language Processing (TASLP), 2019, 27(8), 1280-1294. https://doi.org/10.1109/TASLP.2019.2916360

7. Dragomiretskiy, K, Zosso, D. Variational Mode Decomposition. IEEE Transactions on Signal Processing, 2014, 62(3), 531-44. https://doi.org/10.1109/TSP.2013.2288675

8. Dragomiretskiy, K., Zosso, D. JI. ToSP. Variational Mode Decomposition, 2014, 62(3), 531-44. https://doi.org/10.1109/TSP.2013.2288675

9. Feng Miao, Zhao, R., Jia, L., Wang, X. Multisource Fault Signal Separation of Rotating Machinery Based on Wavelet Packet and Fast Independent Component Analysis. International Journal of Rotating Machinery, 2021. https://doi.org/10.1155/2021/9914724

10. Gelidi, S. D., Seifnaraghi, N., Bardill, A., Wu, Y., Frerichs, I., Demosthenous, A., Tizzard, A., Bayford, R. Towards a Thoracic Conductive Phantom for EIT. Medical Engineering and Physics, 2020, 77, 88-94. https://doi.org/10.1016/j.medengphy.2019.10.008

11. Griffiths, H., Jossinet, J. J. P. M. Bioelectrical Spectroscopy from Multi-frequency. EIT, 1994, 15 Suppl 2a:A59. https://doi.org/10.1088/0967-3334/15/2A/008

12. Hannan, S., Faulkner, M., Aristovich, K., Avery, J., Holder, D. Investigating the Safety of Fast Neural Electrical Impedance Tomography in the Rat Brain. Physiological Measurement, 2019, 40(3), 034003. https://doi.org/10.1088/1361-6579/ab0d53

13. Inany, H. S., Rettig, J. S., Smallwood, C. D., Arnold, J. H., Walsh, B. K. Distribution of Ventilation Measured by Electrical Impedance Tomography in Critically Ill Children. Respiratory Care, 2020, 65(5), 590-595. https://doi.org/10.4187/respcare.07076

14. Jutten, C., Herault, J. J. S. P. Blind Separation of Sources, Part I: An Adaptive Algorithm Based on Neuromimetic Architecture, 1991, 24(1), 1-10. https://doi.org/10.1016/0165-1684(91)90079-X

15. Khan, T. A., Ling, S. H. J. A. Review on Electrical Impedance Tomography. Artificial Intelligence Methods and its Applications, 2019, 12(5), 88. https://doi.org/10.3390/a12050088

16. Langkam, S., Deb, A. K. Dual Estimation Approach to Blind Source Separation. IET Signal Processing, 2017, 11(5). https://doi.org/10.1049/iet-spr.2016.0357

17. Li, J. H., Joppek, C., Faust, U. Fast EIT Data Acquisition System with Active Electrodes and Its Application to Cardiac Imaging. Physiological Measurement, 1996, 17 Suppl 4A. https://doi.org/10.1088/0967-3334/17/4A/005

18. Lu, J., Cheng, W., Zi, Y. Online Blind Source Separation Method with Adaptive Step Size in Both Time. Measurement Science and Technology, 2020, 31(4), 045102. https://doi.org/10.1088/1361-6501/ab5c75

19. Markus, J., David, H. Correction of Electrode Modelling Errors in Multi-Frequency EIT Imaging. Physiological Measurement, 2016, 37(6), 893. https://doi.org/10.1088/0967-3334/37/6/893

20. Mathieu, D., Antoine, D., Chunhui, D., Guillaume, R., Salah, B., Cédric, B. On the Implementation of Simultaneous Multi-Frequency Excitations and Measurements for Electrical Impedance Tomography. Sensors (Basel, Switzerland), 2019, 19(17), 3679. https://doi.org/10.3390/s19173679

21. Moon, D. S., Huh, J. W., Hong, S. B., Koh, Y., Lim, C. M. Dynamic Inhomogeneity of Aeration Along the Vertical Axis of the Lung May Predict Weaning Failure Regardless of Diaphragm Dysfunction. Journal Of Critical Care Medicine, 2021, 65, 186-91. https://doi.org/10.1016/j.jcrc.2021.06.010

22. Oh, T. I., Wi, H., Kim, D. Y., Yoo, P. J., Woo, E. J. A Fully Parallel Multi-frequency EIT System with Flexible Electrode Configuration: KHU Mark2. Physiological Measurement, 2011, 32(7), 835. https://doi.org/10.1088/0967-3334/32/7/S08

23. Oh, T. I., Woo, E. J., David, H. Multi-frequency EIT System with Radially Symmetric Architecture: KHU Markl. Physiological Measurement, 2007, 28(7), S183. https://doi.org/10.1088/0967-3334/28/7/S14

24. Oliveira, B. R. D., Duarte, M. A. Q., Filho, J. V. Blind Source Separation by Multiresolution Analysis using AMUSE Algorithm. Multi-Science Journal, 2018, 1(3), 40-45. https://doi.org/10.33837/msj.v1i3.106

25. Pandey, P., Seeja, K. R. Subject Independent Emotion Recognition from EEG using VMD and Deep Learning. Journal of King Saud University - Computer and Information Sciences, 2019.

26. Pleszczynski, M. Implementation of the Computer Tomography Parallel Algorithms with the Incomplete Set of Data. PeerJ Computer Science, 2021, 7, e339. https://doi.org/10.7717/peerj-cs.339

27. Poni, R., Neufeld, E., Capstick, M., Bodis, S., Samaras, T., Kuster, N. Feasibility of Temperature Control by Electrical Impedance Tomography in Hyperthermia. Cancers (Basel), 2021, 13(13). https://doi.org/10.3390/cancers13133297

28. Schöbi, R., Sudret, B. Structural Reliability Analysis for p-boxes Using Multi-level Meta-models. Probabilistic Engineering Mechanics, 2017, 48, 27-38. https://doi.org/10.1016/j.probengmech.2017.04.001

29. Singh, G., Anand, S., Lall, B., Srivastava, A., Singh, H., (Eds.). Practical Phantom Study of Low Cost Portable EIT Based Cancer Screening Device, 2016 IEEE Long Island Systems, Applications and Technology Conference (LISAT), 2016. https://doi.org/10.1109/LISAT.2016.7494151

30. Soundappan, P., Nikolaidis, E., Haftka, R. T., Grandhi, R., Canfield, R. Comparison of Evidence Theory and Bayesian Theory for Uncertainty Modeling. Reliability Engineering & System Safety, 2004, 85(1-3), 295-311. https://doi.org/10.1016/j.ress.2004.03.018

31. Susana, A. S., Michael, C., Jakob, O., Nadine, H., Steffen, L. Lung Pathologies Analyzed with Multi-frequency Electrical Impedance Tomography: Pilot animal study. Respiratory Physiology & Neurobiology, 2018, 254. https://doi.org/10.1016/j.resp.2018.03.016

32. Tan, C., Liu, S., Jia, J., Dong. F. A Wideband Electrical Impedance Tomography System Based on Sensitive Bioimpedance Spectrum Bandwidth. IEEE Transactions on Instrumentation and Measurement, 2020, 69(1), 144-154. https://doi.org/10.1109/TIM.2019.2895929

33. Wang, C., Wang, Q., Cao, Y. Blind Source Separation Algorithm for Convolution Mixed Signals. IIETA, 2017, 4(4), 103-107. https://doi.org/10.18280/rces.040401

34. Wang, Y.-Q., Zhao, P.-F., Fan, L.-F., Zhou, Q., Wang, Z.-Y., Song, C., et al. Determination of Water Content and Characteristic Analysis in Substrate Root Zone by Electrical Impedance Spectroscopy. Computers and Electronics in Agriculture, 2019, 156, 243-53. https://doi.org/10.1016/j.compag.2018.11.037

35. Weigand, M., Kemna, A. Multi-frequency Electrical Impedance Tomography as a Non-invasive Tool to Characterize and Monitor Crop Root Systems. Biogeosciences, 2017, 14(4), 921-939.. https://doi.org/10.5194/bg-14-921-2017

36. Witkowska-Wrobel, A., Aristovich, K., Faulkner, M., Avery, J., Holder, D. Feasibility of Imaging Epileptic Seizure Onset with EIT and Depth Electrodes. NeuroImage, 2018, 173, 311-321. https://doi.org/10.1016/j.neuroimage.2018.02.056

37. Yadav, I. C., Shahnawazuddin, S., Pradhan, G. Addressing Noise and Pitch Sensitivity of Speech Recognition System Through Variational Mode Decomposition Based Spectral Smoothing. Digital Signal Processing, 2018. https://doi.org/10.1016/j.dsp.2018.12.013

38. Yang, Y. Advanced Digital Electrical Impedance Tomography System for Biomedical Imaging. ERA, 2018.

39. Zhang, X., Zhao, Z., Jia, R., Cao, L., Palma, R. Identification of Microseismic Signals Based on Multiscale Singular Spectrum Entropy. Shock and Vibration, 2020. https://doi.org/10.1155/2020/6717128

40. Zhao, D., Ren, C., Hong, S., Li, Z., Wei, W. J. I. A FPGA-based Sweep-frequency Voltage Source for EIT System. 2010 International Conference on Electronics and Information Engineering, 2010, V2-264-V2-267. https://doi.org/10.1109/ICEIE.2010.5559778